Nanoscale

Accepted Manuscript

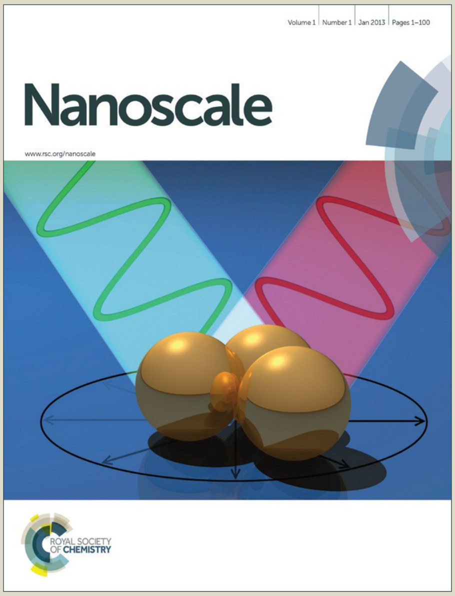

ROYAL SOCIETY OF CHEMISTRY

www.rsc.org/nanoscale

Nanoscale RSCPublishing

PAPER

Cite this: DOI: 10.1039/x0xx00000x

Received 00th January 2012,
Accepted 00th January 2012

DOI: 10.1039/x0xx00000x

www.rsc.org/

Design, fabrication and charge recombination analysis of interdigitated heterojunction nanomorphology on P3HT/PC$_{70}$BM solar cells†

Victor S. Balderrama,[a,b] Josep Albero,[c] Pedro Granero,[a] Josep Ferré-Borrull,[a] Josep Pallarés,[a] Emilio Palomares[d,e] and Lluis F. Marsal *[a]

In this work interdigitated heterojunction photovoltaic devices were manufactured. The donor layer of P3HT nanopillars was fabricated by soft nanoimprinting using nanoporous anodic alumina templates. Subsequently, the PC$_{70}$BM acceptor layer was deposited by spin coating on top of the P3HT nanopillars using a solvent that would not dissolve any of the previous material. Anisole solvent was used because it does not dissolve the bottom donor layer of nanopillars and provides a good wettability between the two materials. Charge extraction was used to determine the charge carrier densities n on the interdigitated heterojunction under operating conditions. Moreover, transient photovoltage measurements were used to find the recombination rate constant in combination with the charge carrier density. At the same time, the interdigitated structure was also compared with the bulk heterojunction and bilayer solar cells manufactured with the same polymeric and fullerene materials in order to understand the recombination loss mechanisms in the ordered and disordered nanomorphology of the active layers.

1. Introduction

In recent years intense efforts has been put into developing organic solar cells (OSC) that are at least as effective cost as the market dominant silicon solar cells. The advantages of their low cost, light-weight, large area, flexibility and ease of processing make organic materials an attractive target.[1-3] The power conversion efficiency of photovoltaic devices has been improved by designing and synthesizing new materials with low band-gaps, changing the structure of devices[3, 4], controlling the nanoscale morphology with additives, applying thermal or solvent annealing, controlling evaporation with solvents [5,6] to increase the interfacial area between donor and acceptor[7], and making nanostructure morphologies such as nanogratings, nanopillars, nanorods and nanodots.[4, 8-12]

In order to improve the performance parameters, nanostructured morphologies have been fabricated with a standard configuration layered with poly (3-hexylthiophene) (P3HT)/[6,6]-phenyl-C61-butyric acid methyl (PCBM), with power conversion efficiencies reported between 1.1-3.25%.[10, 11, 13-17]

It is well known that power conversion efficiency is limited, among other factors by the diffusion length of excitons in the photoactive layer after they have been generated (typically this length is in the range of tens of nanometers in most organic semiconductors).[18-20] To prevent the loss of excitons before dissociation it is necessary to have well defined the morphology of the interfaces between polymer-fullerene materials with equal distances to diffusion length. The free electrons and holes after the exciton dissociation, they are transported by their corresponding material and collected at the metal electrodes. This morphology is known as bulk heterojunction. [21-23]

One promising way to increase the power conversion efficiency of polymer photovoltaic cells is to fabricate well-controllable ordered interdigitated heterojunction nanomorphology (IHJN) by soft nanoimprinting. The excitons generated inside of this nanomorphology can move at the interface to dissociate into electrons and holes and nearly all the free charge carriers can travel along the uninterrupted pathway of the material until they reach their respective electrodes. The vertical IHJN allows the domains in the p-type donor material

[a] Departament d'Enginyeria Electronica, Electrica i Automatica, University of Rovira i Virgili, Països Catalans 26, 43007 Tarragona, Spain, E-mail: lluis.marsal@urv.cat
[b] Sección de Electrónica del Estado Sólido, Departamento de Ingeniería Eléctrica, CINVESTAV, Av. IPN No. 2508, 07360, D.F., Mexico
[c] Institute of Chemical Technology of Valencia (ITQ) Avenue De los Naranjos s/n, 46022 Valencia, Spain
[d] Institute of Chemical Research of Catalonia (ICIQ) Països Catalans 24, 43007 Tarragona, Spain
[e] ICREA. Passeig Lluís Companys, 23, 08010 Barcelona, Spain

†Electronic supplementary information (ESI) available. See DOI: 10.1039/x0xx00000x

and the n-type acceptor material to be aligned normal to the electrode surfaces, thus increasing their crystallinity and charge carrier mobility and reducing recombination rates inside the device.[19, 24, 25] The main progress in IHJN has been achieved by new fabrication techniques and technologies. The interdigitated nanostructures can be manufactured by nanoimprinting lithography (NIL)[26], solvent-assisted nanoimprinting lithography (SANIL)[11], electron-beam lithography (EBL)[17], spin-coating and nanoimprinting template-based methods[13, 16, 27], among many others.[4, 8, 28-32]

Here we report the use of the nanoimprinting method in which nanoporous anodic alumina templates (NAATs) are used to fabricate interdigitated nanostructures in a cost effective and straightforward fashion.[27] NAATs are widely used as template material because they are porous have a good hexagonal order and the geometric characteristics can be easily controlled.[33-35] NAATs and soft nanoimprinting can be combined to provide the vertical nanostructured polymer and the temperature, pressure, and time of the imprint can be precisely controlled.[15, 28, 36] In order to get the complete IHJN structure for OSC application, we used the combination of spin coating and soft nanoimprinting by NAATs to obtain conformal thin films of nanopillars (NP) as donor layer, which made it possible to fabricate several P3HT/$PC_{70}BM$ solar cell devices after the P3HT–NP had been infiltrated with $PC_{70}BM$. Anisole (C_7H_8O) solvent was used to dissolve the fullerene without destroying the donor layer. Bulk heterojunction (BHJ) and bilayer (BL) organic solar cells were fabricated for purpose of comparison with interdigitated solar cells. The fabrication process and conditions were very similar to those of the interdigitated cells.

Once the photovoltaic device with IHJN had been obtained, we need to understand the physical processes involved in device operation. The typical electrical characterization as current–voltage (*J*–*V*) is not enough to understand the solar cell limitations. Some key parameters for better understanding the factors that limit the power conversion efficiency are the charge density distribution and the charge recombination dynamics.
Herein, we apply the charge extraction (CE) and transient photovoltage (TPV) measurements to the IHJN solar cell under steady state operating conditions with the aim of analyzing and determining the charge densities, the carrier recombination dynamics and carrier lifetime dependency on voltage. These measurements are often used in research on BHJ solar cells[37-39] and dyes sensitized solar cells[40], but have not previously been applied to interdigitated structures. Indeed, all the results obtained from the optoelectronic techniques used in this study (CE and TPV) reveal that its interdigitated device nanomorphology is a determining geometric factor that directly affects the charge carrier density, recombination losses and FF during device operation.

2. Experimental section

2.1 Materials

ITO-coated glass substrates (with a nominal sheet resistance of 15 ohm/square and a thickness of 120 nm) were purchased from PsiOTec Ltd. PEDOT:PSS FHC was acquired from Ossila Ltd., P3HT (melting point 238 ºC, Mw = 17500 g mol^{-1}, 99.995% regio-regularity) and $PC_{70}BM$ (M_w = 1031.0 g mol^{-1}) were purchased from Sigma-Aldrich and Solenne BV, respectively. High-purity (99.99%) silver wire was obtained from Testbourne Ltd., and calcium pellets with high-purity (99.99%) were purchased from Kurt J. Lesker.

2.2 Fabrication of NAAT

The NAAT samples were fabricated by the two-step anodization process. Before anodizing, aluminium (Al) substrates were electropolished in a mixture of ethanol (EtOH) and perchloric acid ($HClO_4$) 4:1 (*v*:*v*) at 20 V for 3 min. After this, the first anodization step was performed in an aqueous solution of oxalic acid ($H_2C_2O_4$) 0.3 M at 40 V and 5ºC for 24 h. Subsequently, the alumina film was selectively dissolved by wet chemical etching in a mixture of phosphoric acid (H_3PO_4) 0.4 M and chromic acid (H_2CrO_7) 0.2 M at 70ºC. Then, the second anodization step was conducted under the same anodization conditions as the first step. The anodization time during this step was adjusted to 60 seconds in order to modify the pore length. Finally, the pore diameter was enlarged by a wet chemical etching procedure in an aqueous solution of H_3PO_4 5 wt%. Subsequently, the NAAT were modified by DPMS (DMS-T22) to reduce the surface energy of the templates, and the reaction mechanism was explained by Krumpfer and co-autors.[55][53] The NAAT were immersed in DPMS at 120^{o}C for 24 h, and then rinsed with toluene, and then acetone, ethanol, and DI water. Finally the substrates were dried with nitrogen.

2.3 Device fabrication

Photovoltaic IHJN–OSC devices were fabricated on pre-cleaned patterned ITO glass substrates. 40 nm PEDOT:PSS was applied to the substrates by spin coating at 3500 rpm for 45 s. The PEDOT:PSS film was annealed at 110 ºC for 20 min. The P3HT solution was prepared in chlorobenzene (C_6H_5Cl) and was then spin-coated onto the PEDOT:PSS / ITO glass under nitrogen and a thin film of P3HT was obtained. Afterwards, the nanoimprinting was optimized and carried out with the NAATs by applying 2 MPa at 60 ºC for 5 min to the previous P3HT layer fabricated to get P3HT–NP. The $PC_{70}BM$ solution was prepared in anisole solvent (C_7H_8O) at 10 mg/ml and was deposited on top of P3HT–NP by spin coating at 3000 rpm to backfill the spaces between the nanopillar arrays and form a continuous $PC_{70}BM$ thin film on top. This process was conducted as rapidly as possible to avoid any possible interfacial mixing.

BHJ–OSC and planar bilayer (BL)–OSC were manufactured for purposes of comparison with the IHJN-OSC. BL–OSCs were fabricated under the same conditions as the IHJN–OSC, but without the nanoimprinting process.

BHJ-OSCs were manufactured using the same ITO substrates and PEDOT:PSS layer as for the IHJN. A blend of P3HT:$PC_{70}BM$ (ratio 1:1) was prepared in chlorobenzene (CB) solution and then stirred for 18 h at 40 ºC. The active layer was deposited by spin coating at 600 rpm for 45 s. Afterwards, all the structures (i.e. IHJN–OSC, BHJ–OSC and BL–OSC) were deposited the metal contact by evaporation through a shadow to give devices with an active area of 0.09 cm^2. Ca (20 nm) and Ag (100nm) were deposited at a rate of 0.15 Å s^{-1} and 0.5–0.8 Å s^{-1} respectively. Then, a post-processing annealing was carried out by heating at 130^{o}C for 20 min.

2.4 NAAT Structures characterization

The NAAT samples and IHJN–OSC, BHJ–OSC and BL–OSC structures were characterized by environmental scanning electron microscopy (ESEM FEI Quanta 600). The standard image processing package (ImageJ, a public domain program developed at the RSB of the NIH, USA) was used to carry out the ESEM image analysis. Photoluminescence (PL) was measured in a fluorescence spectrophotometer from Photon Technology International Inc. for the three kinds of structures. A Xe lamp was used as the excitation light source at room temperature with an excitation wavelength (λ_{ex}) of 510 nm and an emission spectrum at an angle of 20º. The absorption spectrum was measured for the three sets of IHJN, BHJ and BL structures at room temperature with a Perkin Elmer Lambda 950 UV/VIS/NIR spectrometer. Atomic force microscopy (AFM Agilent 6400) was used to make several characterizations of the surface morphology of IHJN, BHJ and BL layer structures in the tapping mode.

2.5 Device testing

The *J–V* characteristics of the devices were measured at room temperature using a Keithley 2400 source measurement unit in combination with a solar simulator (Abet Technologies model 11000 class type A, Xenon arc), automatically controlled with a computer. Appropriate filters were used to reproduce the AM 1.5G spectrum. A light intensity of 100 mW/cm^2 was applied to test the organic solar cell devices under illumination. The light intensity was calibrated with an NREL certified monocrystalline silicon photodiode. Film thicknesses were measured by a Dektak 150 surface profilometer. In addition, J–V dark curves were recorded for all the photovoltaic devices.

The CE was used to determine the distribution of charge carrier densities (n) in devices under different conditions of light and voltage. The general CE procedure is to leave the device in open circuit conditions while illuminated at different intensities. Then, the device is shorted while simultaneously turning off the light, and the resulting discharging current transient through a small external load resistor is measured. The desired illumination intensity is achieved with a white light LED ring from LUXEON® Lumileds connected to a DC power supply and a TGP110 function generator that allows the LEDs to reach a background illumination up to 1 sun on the ITO side of the device. The LEDs were typically turned on for approximately 100 ms so that they could reach steady state conditions. The LEDs have a rise/fall time of <100 ns. After the light is switched off and the circuit is temporally closed, while charges are forced to pass through a TDS 2022 oscilloscope from Tektronix© that records the drop in voltage across a resistance of 50 Ω.

In TPV measurements, devices are connected to the 1MΩ input terminal of a Tektronix© TDS2022 oscilloscope and the background illumination was obtained from a ring of 6 white LEDs from LUXEON®. The small perturbation (5mV) was applied through a light pulse (N_2 laser nominal wavelength, 50 ns pulses). The charge recombination rate was calculated for illumination intensities ranging from 0.1 sun to 1 sun.

3. Results and discussion

The preparation of NAAT was carried out by the two-step anodization process as was described in experimental section.[33,34] The pore length was controlled by the anodization time and the pore diameter was enlarged by a wet chemical etching procedure after anodization. The pore diameter (ϕ_p), pore length (H_p) and interpore distance (d_{int}) were 60±4 nm, 80±5 nm and 100±4 nm, respectively. A total of twenty NAAT samples were manufactured and analyzed. The fabrication conditions of the NAAT sample are summarized in Table S1 and showed in Fig. S1 of the Electronic Supplementary Information (ESI). The NAATs were modified by dimethylpolysiloxane (DPMS) to reduce the surface energy of the templates as was described in the experimental section. The results showed that they became more hydrophobic, as was reported.[16] Fig. S2 (a), (b) and (c) from (ESI) show the top-view, tilt-view and cross section-view provided by environmental scanning electron microscopy (ESEM) images of the NAATs after fabrication with oxalic acid electrolyte ($H_2Cr_2O_7$).

Fig. 1 (a-g) show the preparation of IHJN–OSC based on P3HT–NP arrays. The fabrication process of the IHJN–OSC first required P3HT to be deposited on a structure prepared from poly-(ethylene dioxythiophene) doped with poly-(styrene sulphonic acid) (PEDOT:PSS) / indium tin oxide (ITO) as is shown in Fig. 1(a).

The thickness of the P3HT layer was measured by profilometry to be of 130 nm. Then, a soft nanoimprinting process was applied to the prepared NAATs with an antiadhesion layer to imprint the polymer. Hydraulic charge pressure was applied in combination with temperature to produce nanopillars on the P3HT layer. Finally, the template is released from the sample, and polymer nanoimprinting with negative replication of the template is obtained (see Fig. 1(b)). We optimized the soft nanoimprinting conditions (i.e. time, pressure and temperature) to ensure the fidelity of the nanoporous patterns from the NAAT for the P3HT nanopillars as was described in the experimental section. The geometric parameters that define P3HT–NP are the pillar diameter (ϕ_{pillar}), pillar height (H_{pillar}), interpillar distance (S_{pillar}) and residual layer (R-L). Fig. 1(c), (d) and (e) show top-view, tilt-view and cross section-view ESEM images of the P3HT–NP, respectively. The P3HT–NP has an average ϕ_{pillar}= 60±4 nm, H_{pillar}= 80±3 nm, S_{pillar}= 100±5 nm and R-L = 40±3 nm with an aspect ratio of 1.3. Subsequently, the $PC_{70}BM$ fullerene material was deposited by spin coating directly on top of the P3HT–NP layer using anisole solution (2 wt%) as is shown in Fig. 1(f). In this study, we chose $PC_{70}BM$ for two reasons. First, the material has relatively strong and broad absorption in the visible range from 400 nm to 700 nm and gives better results in photon harvesting in the active layer than when such other fullerenes as C_{60}, C_{70} and PCBM are used.[41] The literature only reports the interdigitated nanostructures OSC fabricated with C_{60} and PCBM, not with $PC_{70}BM$. Second, $PC_{70}BM$ can be dissolved in anisole solvent and deposited by spin coating onto the P3HT–NP. The spaces between the P3HT nanopillars were filled with the $PC_{70}BM$ mixture and the anisole solvent. The nanoimprinting polymer layer was not destroyed when the mixture was deposited.[42, 43] Dichloromethane (CH_2Cl_2) has sometimes been used to dissolve the PCBM and fabricate the nanostructured OSC.[10, 16, 17] Anisole is another solvent that may potentially be used for the fabrication of nanostructured cells. Some reports about of anisole solvent has been used to fabricate organic thin film transistors (OTFT) where the various polymer layers have to be deposited using orthogonal solvents.[42, 44] In this study, it is worth noting that $PC_{70}BM$ is used in combination with anisole solvent. It is the first time that this method has been used to deposit $PC_{70}BM$ into the gaps in the P3HT–NP and get the IHJN–OSC. Subsequently, the samples were placed inside the evaporation chamber, where a thin layer of calcium (Ca) and silver (Ag) were evaporated as a top contact (parameters and condition are given in the experimental section) as is shown in Fig. 1(g).

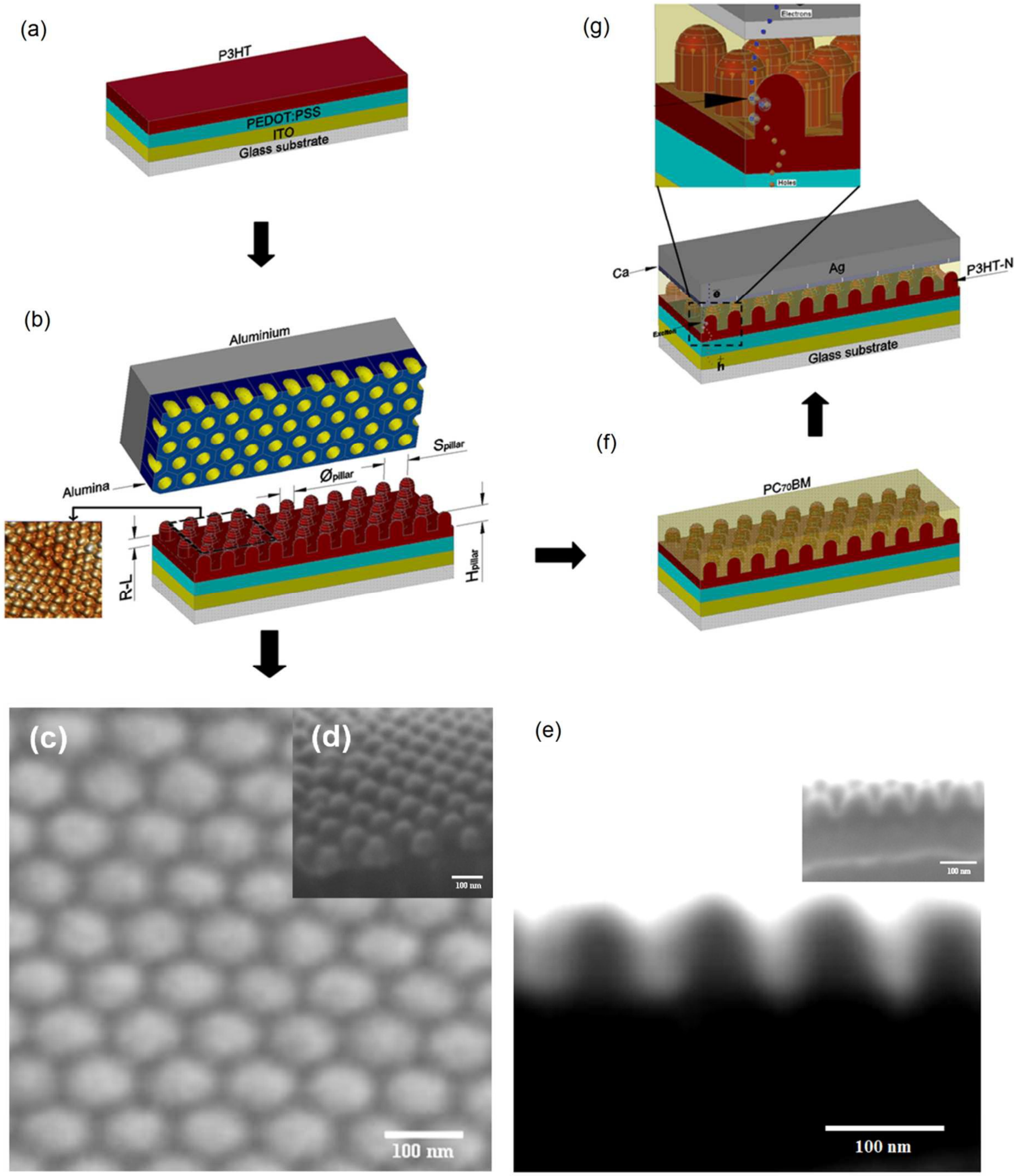

Fig. 1 Different steps to obtain the interdigitated OSC. (a) Spin coating of the P3HT layer on PEDOT:PSS/ITO/Glass. (b) Patterning of P3HT–NP structure done by soft nanoimprinting combining with NAAT templates. The geometrical characteristics of the P3HT–NP can be seen. ϕ_{pillar} is the diameter of the nanopillar, H_{pillar} is the height of nanopillar, S_{pillar} is the distance between nanopillars and R-L is the residual layer of the structure. (c) Top-view of P3HT–NP with excellent replication by soft NAAT applied with ϕ_{pillar} = 60 ± 4 nm. (d) Tilt view and (e) cross section of P3HT–NP with H_{pillar} = 80 ± 3 nm, S_{pillar} = 100 ± 5 nm, R-L = 45 ± 3 nm. (f) Deposition by spin coating of $PC_{70}BM$ using anisole solvent on the P3HT–NP. (g) Deposition of calcium and silver by thermal evaporation on the previous layers to obtain the IHJN–OSC.

Fig. 2(a) shows the cross section-view of the IHJN–OSC structure captured by ESEM. On some samples infiltrated with the fullerene material (P3HT–NP/$PC_{70}BM$) Ca (20nm) and one thin layer of Ag (10 nm) were deposited so that the stack material covered the top surface of the previous active layer, (see Fig. 2(b)). Finally, Fig. 2(c) shows the top view of the top surface of the Ag metal contact with a thickness of 100 nm.

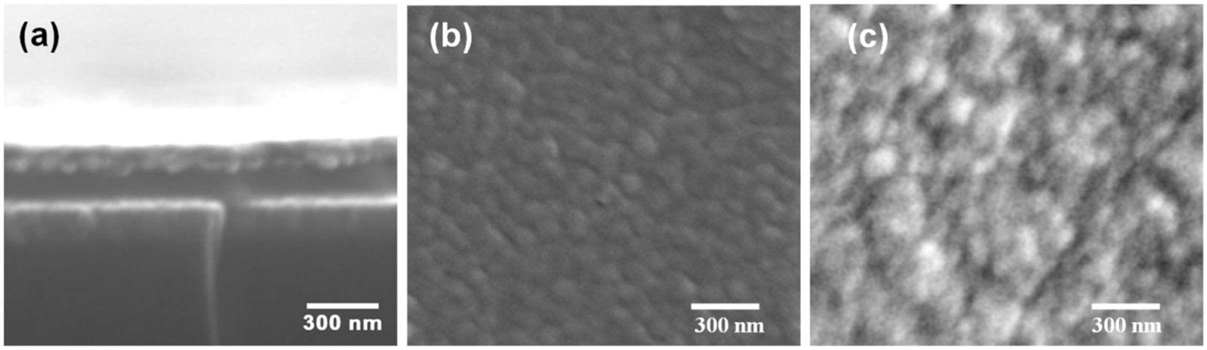

Fig. 2 (a) ESEM images from the cross section of IHJN–OSC with the stack ITO/PEDOT:PSS/P3HT–nanopillar/$PC_{70}BM$/Ca/Ag. (b) Top view after the evaporation of Ca (20 nm) and Ag (20 nm) onto the surface of $PC_{70}BM$/P3HT–nanopillars, (c) Top view of the Ca/Ag metal contact with a thickness of 20 nm/100 nm, respectively.

Two types of control cells based on BHJ–OSC standard blend films (by spin coating from a mixture solution) and BL–OSC (by non-patterned imprinting) were fabricated for purposes of comparison (parameters and conditions are given in the experimental section). The BHJ–OSC has the architecture ITO/PEDOT:PSS/P3HT:$PC_{70}BM$/Ca/Ag and BL–OSC has the stack ITO/PEDOT:PSS/P3HT/$PC_{70}BM$/Ca/Ag.

Atomic force microscopy (AFM) in tapping mode was applied to P3HT–NP, P3HT:$PC_{70}BM$–BHJ and P3HT–single layers after thermal annealing, in order to get further insight into their respective surface areas (see Fig. S3 in ESI).

Fig. 3(a) shows the UV-vis spectroscopy for the pristine P3HT–NP, P3HT flat film and P3HT/$PC_{70}BM$–IHJN, P3HT:$PC_{70}BM$–BHJ and P3HT/$PC_{70}BM$–BL films where were studied. In the UV-vis spectrum, we see that the absorbance of P3HT nanopillar films is 13% higher than that of P3HT flat film at 510 nm, which is consistent with previous reports.[11, 13] A small red-shift was observed for the imprinted film compared to the flat film. Moreover, imprinted P3HT–NP showed a pronounced increase in the shoulder centered at ~ 605 nm, the intensity of which is correlated with the degree of P3HT crystallinity. This is attributed to the fact that P3HT has a greater conjugation length and more ordered structure than the P3HT flat film because of the self -organization of the mobile chains is done during the heating and imprinting of the film compared to P3HT flat film.[24] Thermal annealing was applied during and after imprinting and mainly helped to remove residual solvent and reduce the free volume, which led to closer packing of the polymer chains and improved holes mobility.[45] To enhance the absorbance when nanopillars were used, the geometry had to be optimum (i.e. pillar diameter, pillar height and interpillar distance) so that the light trapping ability inside the structure was also optimum as some simulations have shown.[46] The UV-vis spectrum also shows P3HT/$PC_{70}BM$–IHJN, P3HT:$PC_{70}BM$–BHJ and P3HT/$PC_{70}BM$–BL films with the deposited fullerene material and absorption are observed to be stronger at 490 nm and 380 nm corresponding to the P3HT and $PC_{70}BM$ materials, respectively. P3HT:$PC_{70}BM$–BHJ showed the highest absorption while P3HT/$PC_{70}BM$–BL presented the lowest. This was due to the fact that active layer of BHJ presented a film thickness 200 ± 10 nm, while the active layer of IHJN and BL were 160± 5 nm and 170± 5 nm, respectively. The absorbance peak intensity of P3HT/$PC_{70}BM$–IHJN film was 9% greater than that of P3HT/$PC_{70}BM$–BL film. Moreover, P3HT/$PC_{70}BM$–IHJN showed a considerably higher absorbance (at 600 nm) than that for P3HT:$PC_{70}BM$–BHJ film. The PL measurements for all the structures are shown in Fig. S4 and explained in ESI.

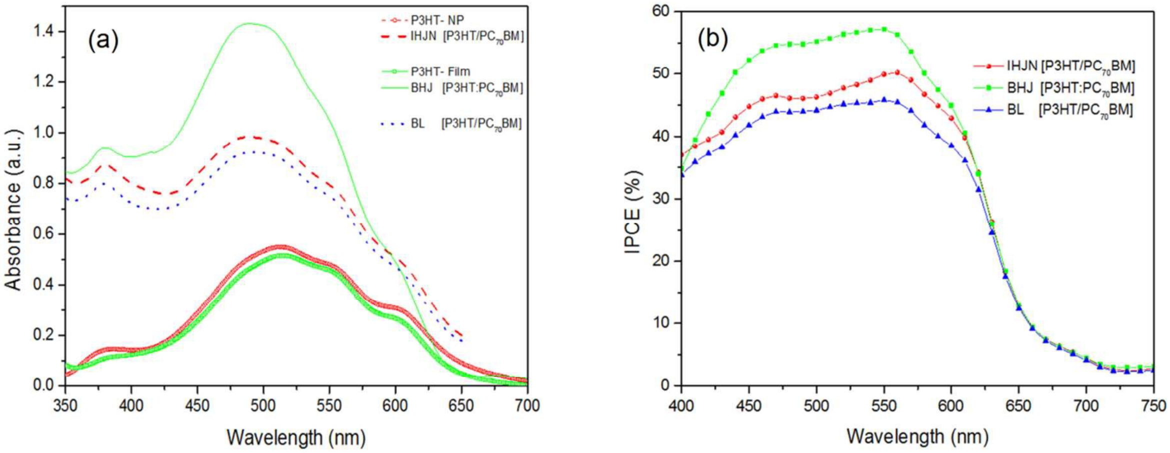

Fig. 3 (a) UV/Visible absorbance of P3HT nanopillars (red open circles) and P3HT– film (green open square). The absorbance spectrum of IHJN–[P3HT/$PC_{70}BM$] (red dashed line), BHJ–[P3HT:$PC_{70}BM$] (green continuous line) and BL–[P3HT/$PC_{70}BM$] (blue dotted line is also shown). (b) IPCE spectrum of IHJN–OSC, BHJ–OSC and BL–OSC.

Fig. 3(b) compares the incident photon to current efficiency (IPCE) spectra for the devices with P3HT/PC$_{70}$BM–IHJN, P3HT:PC$_{70}$BM–BHJ and P3HT/PC$_{70}$BM–BL OSC. It is observed that the trend of the IPCE spectra is similar to that of absorption spectrum throughout the range but particularly between 400 nm and 700 nm. The IPCE of P3HT/PC$_{70}$BM–IHJN, P3HT:PC$_{70}$BM–BHJ and P3HT/PC$_{70}$BM–BL organic solar cells at 550 nm were 50%, 57% and 45%, respectively. By integrating the IPCE curves were determined the short circuit current density for P3HT/PC$_{70}$BM–IHJN, P3HT:PC$_{70}$BM–BHJ and P3HT/PC$_{70}$BM–BL and they were of 6.99 mA/cm^2, 7.67 mA/cm^2 and 6.7 mA/cm^2, respectively which are strongly supported by *J–V* characteristics as it will see below.

Fig. 4(a) illustrates the current–voltage (*J–V*) characteristics of P3HT/PC$_{70}$BM–IHJN imprinted solar cells in comparison to P3HT:PC$_{70}$BM–BHJ and P3HT/PC$_{70}$BM–BL controls OSC under solar illumination at 1 sun (100 mW cm^{-2}). Table 1 summarizes the best and average performance parameters (i.e. open circuit voltage (V_{OC}), short circuit current density (J_{SC}), fill factor (FF) and power conversion efficiency (PCE) of IHJN–OSC (twenty devices), BHJ–OSC (fifteen devices) and BL–OSC (fifteen devices) after fabrication. The best results of the three structures were analyzed.

IHJN–OSC, BHJ–OSC and BL–OSC showed a PCE of 2.6%, 2.4% and 2.1%, respectively. The V_{OC}, FF and PCE of the IHJN–OSC were 3.5%, 19.3% and 8.3% higher than BHJ–OSC, respectively. On the other hand, the J_{SC} of IHJN–OSC was 7.8% less than that of BHJ–OSC. The PCE of the BHJ–OSCs was a little less than that of IHJN–OSC because the active layer was thicker, so that it could be compared with the others. Moreover, the V_{OC}, J_{SC}, FF and PCE of the IHJN–OSC were 1%, 5%, 23% and 24% higher than BL–OSC, respectively.

In this study, we have observed that the enhancement in the PCE of IHJN–OSC was principally originated by the improvements in FF. While that the FF for BHJ–OSC and BL–OSC were low the values. The increase in the performance yield of the J_{SC} of IHJN–OSC we can argue for two aspects: First, it was attributed to the well-controlled interdigitated heterojunction morphology of both materials (P3HT–NP and PC$_{70}$BM) which increased their interfacial area and the contact between them, and made the exciton dissociation more efficient (to get free electrons and holes). Then, the electrons and holes travel through their respective materials to be collected in the metal contact.[14, 16] Second, another reason for the increase in J_{SC} is that the π-π stacking in the P3HT polymer is better oriented and the crystals better formed throughout the nanopillar. This is due to the induction that the polymer undergoes when it is introduced into the nanopore of the template during the soft imprinting step. Therefore, the charge carriers (holes) will move through the P3HT structure and the nanopillar with less difficulty.[24] The improvement of the crystallinity favors the charge-mobility of holes and the charge transport along the P3HT–NP pathways and reduces the recombination of charge carriers on the pathways. This hypothesis was confirmed by analyzing the orientations of the nanopillar morphology of molecular P3HT with micro-X-ray diffraction.[27] The P3HT side chains were found parallel with the axial direction of nanopillars, as similar results were also reported by other publications. [19, 24, 29] It should be point out that although the absolute thickness of IHJN–OSC was 10 nm less than that BL–OSC the J_{SC} was slightly greater. Moreover, the J_{SC} in the P3HT:PC$_{70}$BM–BHJ solar cell was highest because the active layer was thicker and so able to absorb more photons.[11]

The increase of superficial area of the P3HT–NP layer with respect to the P3HT flat film is known as the interface enhancement factor (IEF) which was calculated by applying the (eqn (1))[10, 13, 24]:

$$IEF = \frac{2\pi r_{pillar} H_{pillar} + S_o^2}{S_o^2} \qquad (1)$$

where r_{pillar} is the radius of the nanopillar, H_{pillar} is the height of the nanopillar and S_o is the distance between adjacent nanopillars (also called the nanopillar pitch). The P3HT–NP layer had an IEF of 2.5, which means that the surface area increased with respect to that of the P3HT–flat film.

FF was highest for IHJN–OSC (~61.3%) in comparison with BHJ–OSC (~51.4%) and BL–OSC (~49.0%). This increase in FF for IHJN–OSC can be attributed to the nanoimprinted pattern – in which the interface area between the polymer/fullerene material was greater –, the good quality of the cathode-fullerene and anode-polymer interfaces and the

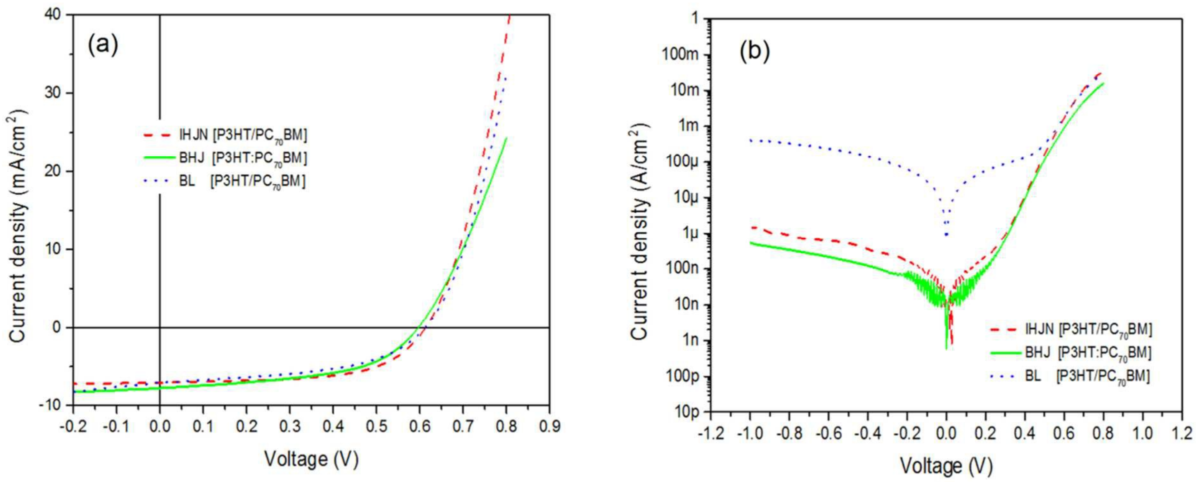

Fig. 4 (a) *J–V* curves to IHJN–OSC (red dashed line), BHJ–OSC (green continuous line) and BL–OSC (blue dotted line) under light (1 sun = 100 mW cm^{-2}). (b) Semi-log *J–V* curve under darkness for the three structures.

Table 1. Device performance based on different morphologies

	P3HT / $PC_{70}BM$	V_{OC}[a] (mV)	J_{SC}[b] (mA cm^{-2})	FF[c] (%)	PCE[d] (%)	$R_{S0\text{-}il}$[e] (Ω-cm^2)	$R_{SH0\text{-}il}$[f] ($k\Omega$-cm^2)	$R_{S0\text{-}dk}$[g] (Ω-cm^2)	$R_{SH0\text{-}dk}$[h] ($k\Omega$-cm^2)
A	IHJN-OSC	613±10	6.4±0.5	53.2±5.6	2.3±0.2	2.58±0.41	0.19±0.06	3.06±0.44	1821.07± 1093.95
B	IHJN-OSC Best	630	7.1	61.3	2.6	2.00	0.26	2.18	603.09
C	BHJ-OSC	594±2	6.8±0.4	50.1±1.2	2.0±0.2	7.71±1.01	0.31±0.02	11.37±2.54	2067.50±634.63
D	BHJ-OSC Best	598	7.7	51.4	2.4	6.62	0.33	8.72	2580.01
E	BL-OSC	569±41	6.5±0.4	43.2±5.1	1.6±0.4	2.93±0.44	0.17±0.04	3.22±0.35	2.11±1.47
F	BL-OSC Best	612	6.8	49.0	2.1	2.43	0.21	2.56	3.60

[a] Open circuit voltage. [b] Short circuit current. [c] Fill factor. [d] Power conversion efficiency. The illumination intensity equivalent applied was 100 m*W*/cm^2 after spectral mismatch correction using AM 1.5G solar simulator. [e] Series resistance per unit area under illumination. [f] Shunt resistance per unit area under illumination. [g] Series resistance per unit area under dark. [h] Shunt resistance per unit area under dark.

decrease in the series resistance (R_S) in the interdigitated heterojunction nanomorphology, all of which suggests that the charge transport properties are substantially improved, as has been observed by other researchers.[9, 37, 47]

Fig. 4(b) shows the *J–V* characteristic in dark conditions for the three organic solar cells. It is well known that R_S can be related to the resistance and thickness of the active layer, the contact resistance between the metal and active layers, the transport properties of the semiconductor material and the properties of the selective contacts. Its value per unit area, R_{S0}, can be calculated by the inversed slope of the *J–V* curve at the highest operating voltage where the curve becomes linear: $R_{S0} = (J / V)^{-1}$, as has been reported in[48, 49]. In this study, the series resistances $R_{S0\text{-}il}$ and $R_{S0\text{-}dk}$ were obtained from the *J–V* characteristic under illumination and darkness, respectively, and the values for each organic solar cell structure are shown in Table 1. In general, $R_{S0\text{-}il}$ and $R_{S0\text{-}dk}$ on IHJN–OSC presented the best values, in which where 70% and 75% lower than for BHJ–OSC and 18% and 15% lower than for BL–OSC, respectively.

The shunt resistance, R_{SH}, which is related to the recombination of charge carriers near the dissociation site (e.g. the donor/acceptor interface of the interdigitated organic materials P3HT–NP/$PC_{70}BM$ in this case) also depends on the transport properties of the semiconductor. The value of shunt resistance per unit area, R_{SH0}, can be determined by calculating the inverse slope around 0 V of the *J–V* curve, $R_{SH0} = (J / V)^{-1}$. In the dark, this parallel shunt resistance is expected to reflect the intrinsic conductivity of the materials. Under illumination, light induced charge generation (photodoping), caused by the charge transfer between the donor and the acceptor, is expected to reduce the shunt dramatically as was observed in our results.[50] In this study, the shunt resistances $R_{SH0\text{-}il}$ and $R_{SH0\text{-}dk}$ were obtained from the *J–V* characteristic under illumination and darkness, respectively and their values are shown in Table 1. Continuing with the analysis, in general, the $R_{SH0\text{-}il}$ and $R_{SH0\text{-}dk}$ of IHJN–OSC were 21% and 76% lower than those of BHJ–OSC, but were 1.23 times and 167 times higher than those of BL–OSC, respectively.

The V_{OC} of IHJN–OSC was 3.5% and 1.1% greater than that of BHJ–OSC and BL–OSC, respectively. The improvement in V_{OC} with respect to the blend devices might be attributed to a reduction in shunt losses, because the wetting layers were correctly arranged in the imprinted devices as reported.[11] It is also reported in the literature that V_{OC} can be attributed to differences in electrical contact work functions and to the difference between the HOMO of the donor and the LUMO of the acceptor.[4, 21] However, when there are recombination losses, the real V_{OC} value depends on the inverse saturation current of the junction in the dark.[50] The V_{OC} value for the IHJN and BL organic solar cells are almost identical. On the other hand, the V_{OC} value for the BHJ-OSC is 6% less than for the IHJN and BL organic solar cells at 1 sun. This must be because in the IHJN and BL cells, the PEDOT:PSS selective electrode is only in contact with the donor material while the calcium selective electrode is in contact with the acceptor material. The donor and acceptor materials of the BHJ cells, however, are in close contact at the same time with both selective contacts.

Table 2 summarizes the method for fabricating nanostructured organic solar cells and compares their geometric characteristics reported in literature with our results.

Table 2. Summary of fabrication method on nanostructured organic solar cells and their geometric characteristics in literature

	Polymer-fullerene	Morphology array	Type of template used[a]	Solvent [b]	Method of manufacture donor- acceptor[c]	Feature size W or ϕ, H, S (nm)[d]	A/A_0 (nm^2)[e]	R-L (nm) [f]	ref.
A	P3HT / C60	Rod	NAAT	-	MW / EV	50, 150, 100	3.3	30	[13]
B	P3HT / PCBM	Rod	NAAT	CH_2Cl_2	NI / SC	50, 80, 100	2.2	20	[10]
C	P3HT / PCBM	Dot	Silicon	$CHCl_3$	SANIL / SC-SANIL	25, 80, 50	3.5	10	[11]
D	P3HT / PCBM	Rod	Silicon	CH_2Cl_2	NI / SC	80, 60, 100	2.5	-	[14]
E	P3HT / PCBM	Nanograting	Silicon	CH_2Cl_2	SANIL / SC	137, 56, 360	1.2	-	[15]
F	P3HT / PCBM	Nanopillar	NAAT	CH_2Cl_2	NI / SC	30, 180, 90	3.0	-	[16]
G	P3HT / PCBM	Nanopillar	-	CH_2Cl_2	EBL / SC	50, 60, 200	1.2	25	[17]
*	P3HT / $PC_{70}BM$	Nanopillar	NAAT	C_7H_8O	NI / SC	60, 80, 100	2.5	40	-

[a] NAAT is nanoporous anodic alumina template [b] Solvents used to dissolve the fullerene material: CH_2Cl_2 is dichloromethane, $CHCl_3$ is chloroform, and C_7H_8O is anisole. [c] MW is melt welting, EV is evaporation, NI is nanoimprinting, SC is spin coating, SANIL is solvent assisted nanoimprint lithography, EBL is electron-beam lithography. [d] W is the width for nanograting morphology or ϕ is the diameter for dot, rot and nanopillars morpholgy, H is the high and S is the pitch or distance between the nanostructures. [e] A/A_0 is the ratio D/A of interface areas of the patterned to the planar-interface photovoltaic devices and this was calculated using eq. (1). [f] Residual layer that is under the nanostructure. * Results from this contribution.

Table 3 Performance summary of nanostructured photovoltaic devices in literature

	Device structure	V_{OC}[a] (mV)	J_{SC}[b] (mA cm^{-2})	FF[c] (%)	PCE[d] (%)	ref.
A	ITO / PEDOT:PSS / P3HT nanorods / C60 (200nm) / LiF (0.6nm) / Al (150nm)	510	4.7	46.0	1.12	13
B	ITO / PEDOT:PSS / P3HT nanorods / PCBM(70 nm) / LiF (0.7nm) / Al (80nm)	570	0.1	56.0	0.05	10
C	ITO / PEDOT:PSS / P3HT nanodots / PCBM (80nm) / Al (80nm)	640	8.6	56.0	3.25	11
D	ITO / PEDOT:PSS / P3HT nanorods / PCBM (70 nm) / Al (100nm)	570	11.3	40.0	2.57	14
E	ITO / PEDOT:PSS / P3HT nanograting / PCBM (69 nm) / Al (100nm)	582	7.6	58.0	2.59	15
F	ITO / PEDOT:PSS / P3HT nanopillars / PCBM (? nm) / Al (100nm)	600	7.4	53.0	2.40	16
G	ITO / PEDOT:PSS / P3HT nanopillars / PCBM (40 nm) / Al (100nm)	600	1.7	40.0	0.43	17
*	ITO / PEDOT:PSS / P3HT nanopillars / PC$_{70}$BM (40 nm) / Ca (20nm) / Ag (100nm)	619	7.1	61.3	2.60	-

[a] Open circuit voltage. [b] Short circuit current. [c] Fill factor. [d] Power conversion efficiency. The Illumination intensity equivalent applied was at 100 m*W* cm^{-2} after spectral mismatch correction using AM 1.5G solar simulator. * Results from this contribution.

Likewise, Table 3 summarizes the performance parameters of the structures shown in Table 2. It is worth noting that our IHJN–OSC is one of the first to be manufactured by spin coating using PC$_{70}$BM and anisole solvent and deposited on P3HT–NP. The fill factor obtained here of 61.3% is higher than all others report in the literature. The PCE of IHJN–OSC was 2.6%, which is comparable with such other standard methods and technologies as standard NIL mold, NAAT and double imprinting.

Fig. 5(a) shows typical CE transients for the devices at 1 sun and in V_{OC} conditions, an extraction half-time of ~8 µs for BHJ–OSC as reported in the literature.[51] For IHJN–OSC and BL–OSC, on the other hand, the half-time was ~6 µs approx.

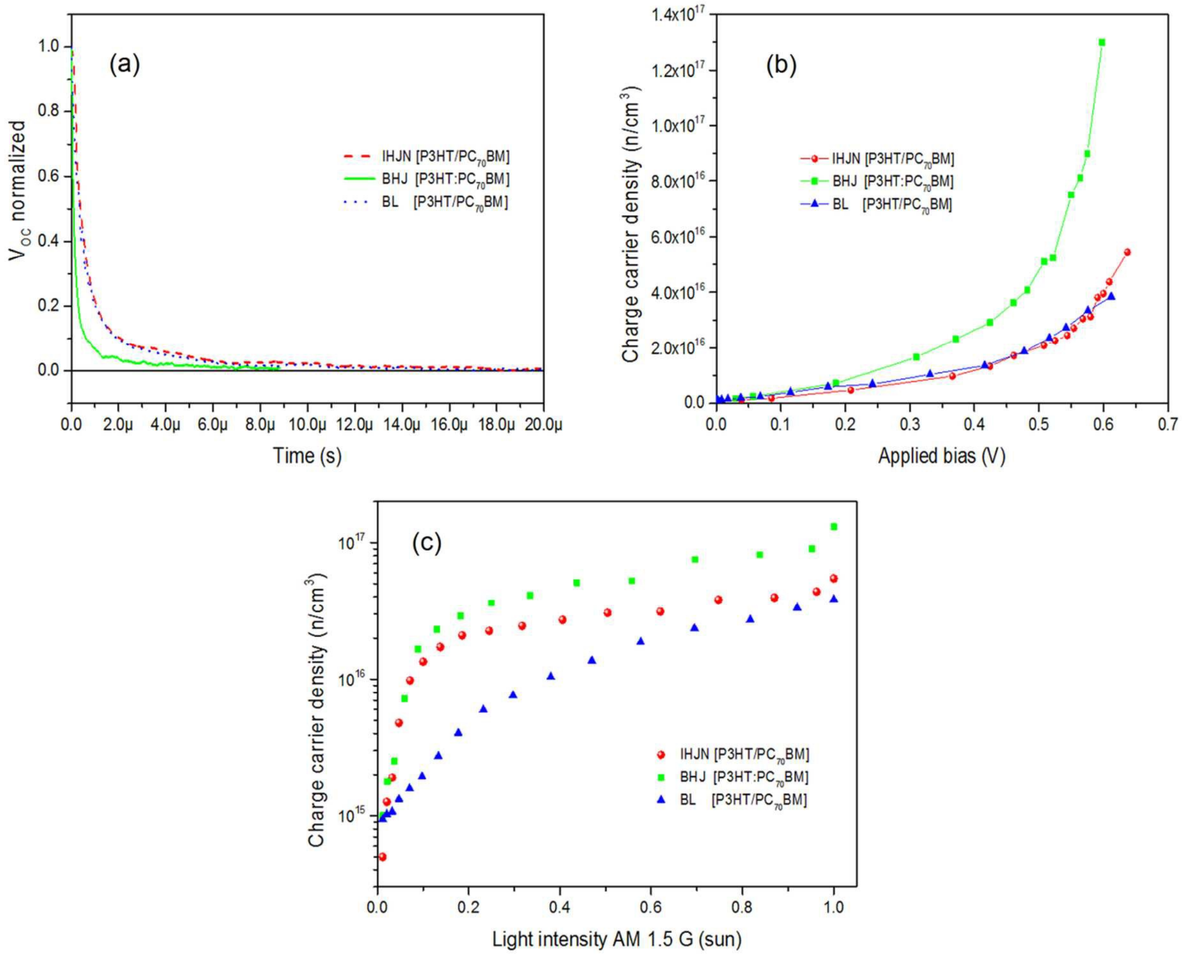

Fig. 5 (a) CE transient acquired to compare IHJN–OSC, BHJ–OSC and BL–OSC under 1 sun steady state background irradiation. For the CE transient, the background irradiation was turned off rapidly, and the device simultaneously switched from open to short circuit. (b) Charge carrier density (*n*) as a function of the applied bias (the maximum point of each curve is 1 sun of light incident on the PV structure during the measurement). In the IHJN–OSC, BHJ–OSC and BL–OSC the charge carrier density undergoes an exponential increase. (c) Log n–light intensity, variation in charge carrier density measured under different light intensities for each structure manufactured.

CE was used to measure the average charge carrier density (n) in the device at various white light intensities while holding the device at V_{OC} and after switching off the light. The light intensities go from dark to 1 sun.

These measurements of n against voltage are shown in Fig. 5(b). Note that this experiment collects charges stored in both the photoactive layer and the electrodes. The extracted charge n at 1 sun on IHJN–OSC, BHJ–OSC and BL–OSC with V_{OC} was ~630 mV, 598 mV and 612 mV where n values were 5.5 x10^{16} cm^{-3}, 1.3 x10^{17} cm^{-3} and 3.8 x10^{16} cm^{-3}, respectively. These values have a stronger correlation with the J_{SC} of the J–V characteristic obtained for each structure analyzed. As have been explained before[51], the charge carrier density in BHJ-OSC manufactured with P3HT:$PC_{70}BM$ can be produced in the bulk of the active layer and at the selective electrodes of the device. Generally, the volumetric charge density in the P3HT:fullerene active layer is more predominant than at the selective electrodes. Our devices with the structure BHJ–OSC, IHJN–OSC and BL–OSC seem to have the same predominant charge accumulation dynamics.[38, 39, 48, 51] Fig. 5(b) and 5(c) show that the charge carrier density in open circuit conditions for different light intensities exponentially depends on the V_{OC} obtained by changing the light intensity according to the following formula (eqn (2))[47]:

$$n_0 = e^{\gamma V_{OC}} \qquad (2)$$

n_0 is the initial charge carrier and γ is a factor related to the presence of energetic disorder in the intrinsic properties of the semiconductor materials. The values of $\gamma < 19\ V^{-1}$ when $p \approx n$, or $\gamma \sim 38\ V^{-1}$ when n>>p or p>>n. Eqn (2) was applied to IHJN–OSC, BHJ–OSC and BL–OSC. n_0 and γ presented values for IHJN–OSC, BHJ–OSC and BL–OSC of 3.58 x 10^{14} cm^{-3} and 9.73 V^{-1}, 4.63 x 10^{14} cm^{-3} and 7.42 V^{-1} and 1.52 x 10^{15} cm^{-3} and 5.29 V^{-1}, respectively. The γ values obtained in this study are similar to the ones obtained in others an in all cases they are less than half of the value expected for an ideal band-gap.[37, 38] This suggests that gamma values present a non-ideal behavior and is due to the presence of an exponential tail of density of trap states extending into the band-gap of the photoactive layer. In other words these traps correspond to the presence of energetic disorder in the active layer, which influences the transport and recombination processes.[47, 52] So, we suggest that the structure with most energetic disorder in the active layer was BL–OSC and the structure with the least was IHJN–OSC.

The TPV measurements were performed on IHJN–OSC, BHJ–OSC, and BL–OSC. The charge carrier density obtained from CE measurements for different light intensities (from 0.3 to 1.0 sun) was used to get the carrier lifetime from TPV measurements. The decay dynamics for all devices agrees with previous measurements on P3HT:PCBM blends: namely, that single-exponential fits apply for a wide range of illumination intensities.[37-39, 47, 48, 53, 54] Fig. 6(a) shows carrier lifetimes as a function of carrier density for varying illumination intensities. At one sun, the IHJN–OSC, BHJ–OSC and BL–OSC have carrier lifetimes of ~3.9 μs, ~5.8 μs and 4.2 μs, respectively. The recombination lifetime decreases when the light intensity is increasing until achieve to 1 sun and the charge carriers are also increasing.

The charge density has an inverse square relationship with the recombination lifetime (eqn (3)) with $\beta/\gamma = \lambda$. IHJN–OSC, BHJ–OSC and BL–OSC show λ values of 2.4, 2 and 1.8, respectively.

$$\tau_{\Delta n} = \tau_{n0}\,(n_0/n)^{\lambda} \qquad (3)$$

All the values of λ indicate there are bimolecular recombinations as similar values were reported in the literature.[37, 39, 48] Fig. 6(b) shows the bimolecular recombination rate constants k_{rec} and were calculated from the carrier lifetimes and densities according to the following eqn (4)[51]:

$$k_{rec} = 1/(\lambda+1)\,\tau_{\Delta n} \qquad (4)$$

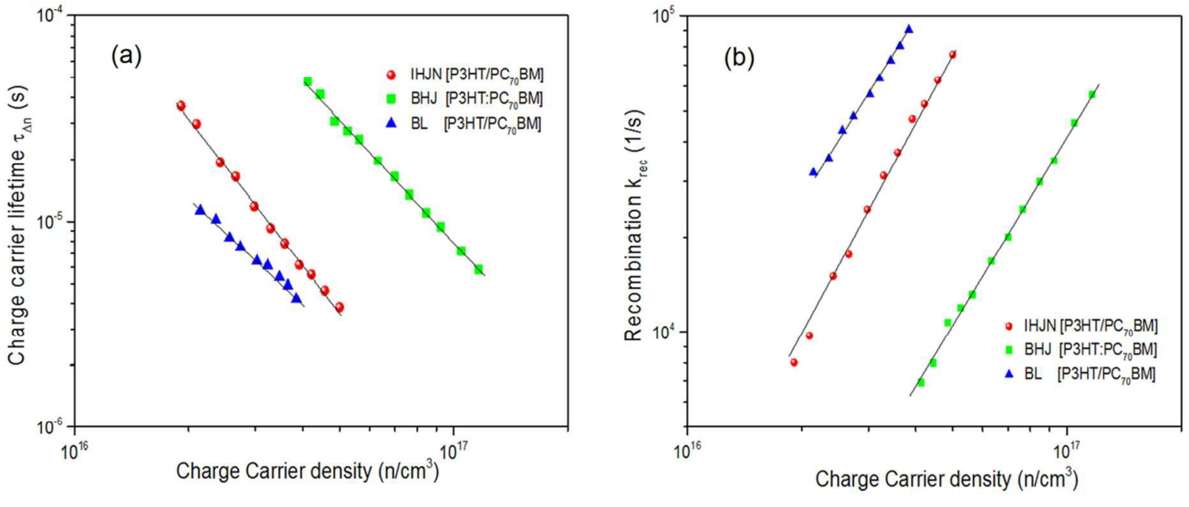

Fig. 6 (a) TPV measurements were performed under open circuit conditions and different illumination (V_{OC}) for IHJN–OSC, BHJ–OSC and BL–OSC structures. (b) Bimolecular recombination rate constant k_{rec}, extracted from carrier τ and n, as a function of n. The pulse excitation wavelength was 470 nm. The pulsed source power was set so that the ΔV of the TPV measurement did not exceed 3% of the V_{OC} measured at 0.1 sun.

The devices with the lowest bimolecular recombination rate were BHJ–OSC. Reduced recombination constants are considered critical for efficient solar cells. BHJ–OSC had the longest carrier lifetimes and smallest k_{rec} values whereas BL–OSC had the shortest carrier lifetimes and largest $k_{rec.}$ IHJN–OSC presented values in between (see Fig. 6(b)).

All the electrical characterization used in this study provides insight into the working mechanisms of the various organic solar cells that were fabricated and analyzed. The critical parameter(s) required to improve the synthesis, design and fabrication on interdigitated organic solar cells and enhance the performance parameters have been identified.

4. Conclusions

In summary, the IHJN–OSC were manufactured by soft nanoimprinting in combination with nanoporous anodic alumina templates to produce P3HT–NP and they were filled by spin coating of $PC_{70}BM$ on the top of NP in combination with anisole orthogonal solvent. The fabrication method, using this orthogonal solvent, on IHJN–OSC has been reported for the first time. The P3HT–NP presented good replication and a well-ordered array of NAAT with an average diameter of 60 nm, pillar height of 80 nm and interpillar distance of 100 nm. IHJN–OSC was compared with BHJ–OSC and BL-OSC as controls and they were fabricated under the same conditions. The surface area of the P3HT–NP increased 2.5 times more than that of BL-OSC. Current–voltage characteristics and optical measurement were applied for all photovoltaic devices. The results provide direct evidence that the imprinting layer gives FF ~ 61.3% and PCE ~2.6%. This due to the larger interface between the donor and acceptor materials, resulting in more efficient photogeneration, exciton dissociation and charge transport on extended interfaces made up of a finely controlled morphology. CE and TPV measurement were applied on IHJN–OSC. Bimolecular recombination was found to be the main mechanism by which charge carriers were lost. For the interdigitated the recombination losses were lower than for BL–OSC. The gamma values for the IHJN–OSC, presented an exponential tail of density of trap states that extended into the band-gap of the photoactive layer. These values were lower for IHJN–OSC than for BHJ–OSC and BL–OSC. In other words, the structure with the lowest energetic disorder in the active layer was IHJN–OSC where the recombination process is reduced. The study of the three structures at the same time provides important information about how such physical properties as the charge density, charge carrier lifetime and mechanism are governed inside the device.

We conclude that interdigitated morphology has a favorable influence on photogeneration and charge transport but they also depend on factors such as the quality of the materials, the fabrication process (e.g. the use of orthogonal solvents, quality of materials, etc.), technology and even how the solar cells are characterized. The use of orthogonal solvents to fabricate solar cells offers a simple, potentially low-cost fabrication route and opens up new possibilities for using new polymers for manufacturing interdigitated OSC.

Acknowledgements

This work was supported by the Spanish Ministry of Economy and competitiveness (MINECO) under grant number TEC2012-34397, the ICREA under the ICREA Academia Award and by Catalan authority under project AGAUR 2014 SGR 1344. EP would like to thank MINECO for the project CTQ2013-47183-R and the support through Severo Ochoa Excellence Accreditation 2014-2018(SEV-2013-0319)

Notes and references

[a] University of Rovira i Virgili, Països Catalans 26, 43007 Tarragona, Spain, E-mail: lluis.marsal@urv.cat

[b]Sección de Electrónica del Estado Sólido, Departamento de Ingeniería Eléctrica, CINVESTAV, Av. IPN No. 2508, 07360, D.F., Mexico

[c] Institute of Chemical Technology of Valencia (ITQ) Avenue De los Naranjos s/n, 46022 Valencia, Spain

[d] Institute of Chemical Research of Catalonia (ICIQ) Països Catalans 24, 43007 Tarragona, Spain

[e] ICREA. Passeig Lluís Companys, 23, 08010 Barcelona, Spain

†Electronic supplementary information (ESI) available. See DOI: 10.1039/x0xx00000x

1. C. J. Brabec, *Sol. Energ. Mater. Sol. Cells*, 2004, **83**, 273-292.
2. V. S. Balderrama, M. Estrada, A. Viterisi, P. Formentin, J. Pallarés, J. Ferré-Borrull, E. Palomares and L. F. Marsal, *Microelectron. Reliab.*, 2013, **53**, 560-564.
3. P. Reiss, E. Couderc, J. De Girolamo and A. Pron, *Nanoscale*, 2011, **3**, 446-489.
4. J.-T. Chen and C.-S. Hsu, *Polym. Chem.*, 2011, **2**, 2707-2722.
5. J. Jo, S.I. Na, S.S. Kim, T.W. Lee, Y. Chung, S.J. Kang, D. Vak and D.-Y. Kim, *Adv. Funct. Mater.*, 2009, **19**, 2398-2406.
6. W. Ma, C. Yang, X. Gong, K. Lee and A. J. Heeger, *Adv. Funct. Mater.*, 2005, **15**, 1617-1622.
7. K. Sivula, Z. T. Ball, N. Watanabe and J. M. J. Fréchet, *Adv. Mater.*, 2006, **18**, 206-210.
8. J. Weickert, R. B. Dunbar, H. C. Hesse, W. Wiedemann and L. Schmidt-Mende, *Adv. Mater.*, 2011, **23**, 1810-1828.
9. X. Li, W. C. H. Choy, L. Huo, F. Xie, W. E. I. Sha, B. Ding, X. Guo, Y. Li, J. Hou, J. You and Y. Yang, *Adv. Funct. Mater.*, 2012, **24**, 3046-3052.
10. W. Wiedemann, L. Sims, A. Abdellah, A. Exner, R. Meier, K. P. Musselman, J. L. MacManus-Driscoll, P. Müller-Buschabaum, G. Scarpa, P. Lugli and L. Schmidt-Mende, *Appl. Phys. Lett.*, 2010, **96**, 263109.
11. X. He, F. Gao, G. Tu, D. G. Hasko, S. Hüttner, N. C. Greenham, U. Steiner, R. H. Friend and W. T. S. Huck, *Adv. Funct. Mater.* , 2011, **21**, 139-146.
12. M. Yu, Y. Z. Long, B. Sun and Z. Fan, *Nanoscale*, 2012, **4**, 2783-2796.
13. J. S. Kim, Y. Park, D. Y. Lee, J. H. Lee, J. H. Park, J. K. Kim and K. Cho, *Adv. Funct. Mater.*, 2010, **20**, 540-545.
14. M. Aryal and F. Buyukserin, *J. Vac. Sci. Technol. B*, 2008, **26**, 2562-2566.
15. J. Y. Park, N. R. Hendricks and K. R. Carter, *Langmuir*, 2011, **27**, 11251-11258.
16. D. Chen, W. Zhao and T. P. Russell, *ACS Nano*, 2012, 6, 1479-1485.
17. S. Moungthai, N. Mahadevapuram, P. Ruchhoeft and G. E. Stein, *ACS Appl. Mater. Interfaces*, 2012, **4**, 4015-4023.
18. C. W. Tang and S. A. Vanslyke, *Appl. Phys. Lett.*, 1987, **51**, 913-915.

19. J. Slota, X. Hea and W. T. S. Huck, *Nano Today*, 2010, 5, 231-241.
20. K. M. Coakley, Y. Liu, C. Goh and M. D. McGehee, *MRS Bull.*, 2005, **30**, 37-40.
21. C. J. Brabec, N. S. Sariciftci and J. C. Hummelen, *Adv. Funct. Mater.*, 2001, **11**, 15-26.
22. H. Hoppe and N. S. Sariciftci, *J. Mater. Chem.*, 2006, **16**, 45-61.
23. V. S. Balderrama, M. Estrada, A. Cerdeira, B. S. Soto-Cruz, L. F. Marsal, J. Pallares, J. C. Nolasco, B. Iñiguez, E. Palomares and J. Albero, *Microelectron. Reliab.*, 2011, **51**, 597-601.
24. Y. Yang, K. Mielczarek, M. Aryal, A. Zakhidov and W. Hu, *ACS Nano*, 2012, **6**, 2877-2892.
25. L. Zhao, S. Zhao, Z. Xu, Q. Yang, D. Huang and X. Xu, *Nanoscale*, 2015, **7**, 5537-5544.
26. Y. Liu, C. Kirsch, A. Gadisa, M. Aryal, S. Mitran, E. T. Samulski and R. Lopez, *J. Phys. D: Appl. Phys.*, 2013, **46**, 024008.
27. A. Santos, P. Formentín, J. Pallarés, J. Ferré-Borrull and L. F. Marsal, *Sol. Energy Mater. Sol. Cells*, 2010, **94**, 1247-1253.
28. J. H. Lee, D. W. Kim, H. Jang, J. K. Choi, J. Geng, J. W. Jung, S. C. Yoon and H.-T. Jung, *Small*, 2009, **5**, 2139-2143.
29. M. Aryal, K. Trivedi and W. Hu, *ACS Nano*, 2009, 3, 3085-3090.
30. A. Greiner and J. H. Wendorff, *Angew. Chem. Int. Ed.*, 2007, **46**, 5670-5703.
31. F. C. Krebs, *Sol. Energy Mater. Sol. Cells*, 2009, **93**, 394-412.
32. N. Haberkorn, J. S. Gutmann and P. Theato, *ACS Nano*, 2009, **3**, 1415-1422.
33. H. Masuda, H. Yamada, M. Satoh and H. Asoh, *Appl. Phys. Lett.*, 1997, **71**, 2770-2772.
34. A. Santos, P. Formentin, J. Pallarés, J. Ferré-Borrull and L. F. Marsal, *Mater. Lett.*, 2010, **64**, 371-374.
35. A. P. Li, F. Müller, A. Birner, K. Nielsch and U. Gösele, *J. Appl. phys.*, 1998, **84**, 6023-6026.
36. D. Cheyns, K. Vasseur, C. Rolin, J. Genoe, J. Poortmans and P. Heremens, *Nanotechnol.*, 2008, **19**, 424016-424021.
37. J. Albero, Y. Zhou, M. Eck, F. Rauscher, P. Niyamakom, I. Dumsch, S. Allard, U. Scherf, M. Kruger and E. Palomares, *Chem. Sci.*, 2011, **2**, 2396-2401.
38. A. Maurano, R. Hamilton, C. G. Shuttle, A. M. Ballantyne, J. Nelson, B. O'Regan, W. Zhang, I. McCulloch, H. Azimi, M. Morana, C. J. Brabec and J. R. Durrant, *Adv. Mater.*, 2010, **22**, 4987-4992.
39. A. Guerrero, N. F. Montcada, J. Ajuria, I. Etxebarria, R. Pacios, G. Garcia-Belmonte and E. Palomares, *J. Mater. Chem. A*, 2013, **1**, 12345-12354.
40. B. C. O'Regan and J. R. Durrant, *J. Phys. Chem. B*, 2006, **110**, 8544-8547.
41. F. Zhang, Z. Zhuo, J. Zhang, X. Wang, X. Xu, Z. Wang, Y. Xin, J. Wang, J. Wang, W. Tang, Z. Xu and Y. Wang, *Sol. Energy Mater. Sol. Cells*, 2012, **97**, 71-77.
42. M. Estrada, I. Mejia, A. Cerdeira and B. Iñiguez, *Solid-State Electron.*, 2008, **52**, 53-59.
43. J. S. Jaworski, M. Cembor and M. Orlik, *J. Electroanal. Chem.*, 2005, **582**, 165-170.
44. I. Mejia, M. Estrada and M. Avila, *Microelectron. Reliab.*, 2008, **48**, 1795-1799.
45. F. Padinger, R. S. Rittberger and N. S. Sariciftci, *Adv. Funct. Mater.*, 2003, **13**, 85-88.
46. P. Granero, V. S. Balderrama, J. Ferré-Borrull, J. Pallarès and L. F. Marsal, *J. Appl. Phys.*, 2013, **113**, 043107.
47. A. Maurano, C. G. Shuttle, R. Hamilton, A. M. Ballantyne, J. Nelson, W. Zhang, M. Heeney and J. R. Durrant, *J. Phys. Chem. C*, 2011, **115**, 5947-5957.
48. C. G. Shuttle, B. O'Regan, A. M. Ballantyne, J. Nelson, D. D. C. Bradley, J. de Mello and J. R. Durrant, *Appl. Phys. Lett.*, 2008, **92**, 093311.
49. V. S. Balderrama, M. Estrada, P. L. Han, P. Granero, J. Pallarés, J. Ferré-Borrull and L. F. Marsal, *Sol. Energ. Mater. Sol. Cells*, 2014, **125**, 155-163.
50. C. Waldauf, M. C. Scharber, P. Schilinsky, J. A. Hauch and C. J. Brabec, *J. Appl. Phys.*, 2006, **99**, 104503.
51. C. G. Shuttle, A. Maurano, R. Hamilton, B. O'Regan, J. C. de Mello and J. R. Durrant, *Appl. Phys. Lett.*, 2008, **93**, 183501.
52. C. G. Shuttle, R. Hamilton, J. Nelson, B. C. O'Regan and J. R. Durrant, *Adv. Funct. Mater.*, 2010, **20**, 698-702.
53. C. G. Shuttle, R. Hamilton, B. C. O'Regan, J. Nelson and J. R. Durrant, *Proc. Natl. Acad. Sci.*, 2010, **107**, 16448-16452.
54. I. Etxebarria, A. Guerrero, J. Albero, G. Garcia-Belmonte, E. Palomares and R. Pacios, *Org. Electron.*, 2014, **15**, 2756-2762.
55. J. W. Krumpfer and T. J. McCarthy, *Langmuir*, 2011, **27**, 11514-11519.